Observation of *S*= 1/2 quasi-1D magnetic and magneto-dielectric behavior in a cubic $SrCuTe_2O_6$

2015 J. Phys.: Condens. Matter 27 426001

(http://iopscience.iop.org/0953-8984/27/42/426001)

IOP Publishing Journal of Physics: Condensed Matter

J. Phys.: Condens. Matter **27** (2015) 426001 (10pp) doi:10.1088/0953-8984/27/42/426001

Observation of $S = 1/2$ quasi-1D magnetic and magneto-dielectric behavior in a cubic $SrCuTe_2O_6$

B Koteswararao[1,2,3], S K Panda[4,7], R Kumar[5], Kyongjun Yoo[2], A V Mahajan[5], I Dasgupta[4,6], B H Chen[3], Kee Hoon Kim[2] and F C Chou[3]

[1] School of Physics, University of Hyderabad, Central University PO, Hyderabad 500046, India
[2] CeNSCMR, Department of Physics and Astronomy, and institute of applied physics, Seoul National University, Seoul 151–747, Korea
[3] Center of Condensed Matter Sciences, National Taiwan University, Taipei 10617, Taiwan
[4] Centre for Advanced Materials, Indian Association for the Cultivation of Science, Jadavpur, Kolkata-700032, India
[5] Department of Physics, Indian Institute of Technology Bombay, Mumbai 400076, India
[6] Department of Solid State Physics, Indian Association for the Cultivation of Science, Jadavpur, Kolkata 700 032, India

E-mail: khkim@phya.snu.ac.kr and fcchou@ntu.edu.tw

Received 20 May 2015, revised 9 August 2015
Accepted for publication 7 September 2015
Published 5 October 2015

Abstract

We investigate the magnetic, thermal, and dielectric properties of $SrCuTe_2O_6$, which is isostructural to $PbCuTe_2O_6$, a recently found, Cu-based 3D frustrated magnet with a corner-sharing triangular spin network having dominant first and second nearest neighbor (*nn*) couplings (Koteswararao *et al* 2014 *Phys. Rev.* B **90** 035141). Although $SrCuTe_2O_6$ has a structurally similar spin network, the magnetic data exhibit the characteristic features of a typical quasi-1D magnet, which mainly resulted from the magnetically dominant third *nn* coupling, uniform chains. The magnetic properties of this system are studied via magnetization (M), heat capacity (C_p), dielectric constant (ε'), and measurements along with *ab initio* band structure calculations. The magnetic susceptibility $\chi(T)$ data show a broad maximum at 32 K and the system orders at low temperatures $T_{N1} \approx 5.5$ K and $T_{N2} \approx 4.5$ K, respectively. The analysis of the $\chi(T)$ data gives an intra-chain coupling, J_3/k_B, to be about ≈ -42 K with non-negligible frustrated inter-chain couplings (J_1/k_B and J_2/k_B). The hopping parameters obtained from the LDA band structure calculations also suggest the presence of coupled uniform chains. The observation of simultaneous anomalies in $\varepsilon'(T)$ at T_{N1} and T_{N2} suggests the presence of a magneto-dielectric effect in $SrCuTe_2O_6$. A magnetic phase diagram is also built based on the M, C_p, and ε' results.

Keywords: $SrCuTe_2O_6$, frustration, $S = 1/2$ uniform chains, magneto-dielectric behavior

(Some figures may appear in colour only in the online journal)

1. Introduction

Magnetism in one-dimensional (1D) antiferromagnetic (AFM) $S = 1/2$ systems is very interesting due to their inherent tendency to uphold strong quantum fluctuations, which lead to a ground state (GS) with quasi-long range order (LRO) [1]. In a 1D chain, the involvement of the frustrated next nearest neighbor (*nnn*) coupling (J') to its nearest neighbor (*nn*) coupling (J) exhibits a variety of exotic ground states ranging from spin disordered, gapped states to spin ordered states with

[7] Present address: Department of Physics and Astronomy, Uppsala University, SE-751 20 Uppsala, Sweden.

simultaneous ferroelectric order. The emerging ground states depend on the type as well the strength of these couplings (J and $J^{'}$). For instance, in the case of the $S = 1/2$ AFM chain, when the ratio of the *nnn* to *nn* coupling ($J^{'}/J$) is about 0.5, the resultant GS opens up a spin gap to its first excited state [2]. On the other hand, the involvement of *nnn* AFM coupling to a ferromagnetic (FM) uniform chain also causes competition between these two interactions and induces some nontrivial magnetic orderings such as spiral, helical, etc. Theoretically, the helical magnetic structure has been proposed for $\left|J^{'}/J\right| > 0.25$ [3, 4]. Experimentally, such a state has already been realized for many $S = 1/2$ chain systems, including $LiCu_2O_2$, $LiCuVO_4$, Li_2ZrCuO_4, $CuCl_2$, $CuBr_2$, $CuCrO_4$, etc [5–12]. These are a few well-known examples of ribbon chains made by a CuX_4 plaquette (where $X = O$, Cl, and Br) and possess nontrivial spin structures. Also, ferroelectricity was evidenced for most of the above mentioned systems, except Li_2ZrCuO_4 [13], via a sharp transition in the dielectric constant and the occurrence of a spontaneous electric polarization vector (P) along some crystallographic axis.

The simple inverse Dzyaloshinsky–Moriya (IDM) or spin-current model explains the magneto-electric behavior for such existing non-collinear magnets. However, the observed P value is smaller than the theoretically estimated value in quantum spin systems, which might be the result of quantum fluctuations [14, 15]. This quantum spin-driven multiferroicity has created a lot of excitement at the fundamental research level. In order to understand more about the origin and the mechanism of magneto-electric coupling in frustrated quantum spin chains, a few more varieties of potential magnetic chain systems need to be studied.

Herein, we introduce a new magnetic chain-like system $SrCuTe_2O_6$. This cubic system [16] is isostructural to $PbCuTe_2O_6$ [17]. The first and second *nn* of Cu atoms form a frustrated 3D network, whereas the third *nn* forms a non-frustrated uniform chain. The magnetic properties and heat capacity of $PbCuTe_2O_6$ show the absence of any conventional LRO down to 350 mK, despite the presence of antiferromagnetic correlations with $\theta_{CW} \approx -22$ K. In addition, the heat capacity data exhibit a broad-maximum (T^{max}) at 1.15 K ($T^{max}/\theta_{CW} \approx 0.05$) and a weak-kink at 0.9 K, which rather result from the highly frustrated network in $PbCuTe_2O_6$ as suggested by the structure. The hopping parameters estimated from the LDA calculations also suggest the presence of a 3D frustrated network with considerable additional interactions.

Although the spin arrangement of $SrCuTe_2O_6$ is the same as that of $PbCuTe_2O_6$, the magnetic susceptibility $\chi(T)$ data surprisingly exhibit a broad maximum at 32 K. This qualitatively infers the presence of short-range interactions originating from the magnetically dominant third *nn* couplings (uniform chains). The system undergoes antiferromagnetic (AFM) ordering with the transition temperatures $T_{N1} \approx 5.5$ K and $T_{N2} \approx 4.5$ K, which further suggests the presence of non-negligible frustrated inter-chain couplings (J_1 and J_2). Our LDA calculations also confirm that $SrCuTe_2O_6$ has a network of uniform chains (formed by third *nn*) with various inter-chain AFM couplings. The observation of a cusp-like anomaly in the dielectric constant data and the absence of spontaneous electric polarization (P) together indicate the presence of magneto-dielectric behavior below its T_{N1}. This new kind of uniform chain with magneto-dielectric anomalies in $SrCuTe_2O_6$ might open up a new problem at the theoretical front to understand the mechanism for magneto-dielectric behavior in 1D AFM chain systems with frustrated inter-chain couplings.

2. Experimental details

The polycrystalline samples of $SrCuTe_2O_6$ were prepared by the solid-state reaction method. First a precursor, $SrTe_2O_5$, was prepared by firing the stoichiometric amounts of $SrCO_3$ and TeO_2 at 450 °C for 48 h in air, followed by one intermediate grinding. At the second step, the obtained single phase sample of $SrTe_2O_5$ was mixed with CuO in a molar ratio of 1 : 1 and the pelletized mixture was sealed in an evacuated quartz tube and fired at 650 °C for 72 h. Two intermediate grindings were required to get the single phase sample of $SrCuTe_2O_6$. The powder x-ray diffraction measurements were done at room temperature using a PANalytical X' pert PRO powder diffractometer equipped with Cu Kα radiation. The magnetic measurements were performed in the T-range from 2 to 300 K and in the magnetic field (H) range 0–70 kOe on a Quantum design SQUID-VSM. The heat capacity (C_p) measurements were done using PPMS (Quantum design, Corp.) in the T-range from 2 to 300 K and in the field range from 0 to 90 kOe. To ensure a better thermal contact between the sample and the sample platform, Apiezon N grease was used for the C_p measurements. For the capacitance measurement, the pellet was cut and polished to make a thin plate with a thickness of about 0.3 mm, and the electrical contacts were made on both sides of the pellet by attaching thin copper wires 85 μm thick with silver epoxy. Finally, the capacitance and pyroelectric current were measured using a high precision capacitance bridge (AH 2550 A) and a KE617 electrometer, respectively. These experimental set-ups were attached to PPMS to carry out the measurements as a function of magnetic field (0–90 kOe) and temperature.

3. Results and discussion

3.1. X-ray diffraction and structural features

The $SrCuTe_2O_6$ crystallizes in a cubic space group $P4_132$ (No 213) [16]. Figure 1 shows the measured x-ray diffraction pattern (XRD) of the polycrystalline samples. The atomic coordinates obtained as a result of Rietveld refinement under the Fullprof method are summarized in table 1. The obtained lattice constant by the Fullprof refinement method [18] is to be $a \approx 12.463$ Å and is consistent with the previously reported value of $a \approx 12.472$ Å [16]. The selected bond angles and bond lengths between the Cu atoms are provided in table 2.

As shown in figures 2(a) and (b), the structure of the titled compound consists of CuO_4 square plates, one-end opened TeO_3 units, and the octahedral environments of Sr1 and Sr2. Similar to its sister compound $PbCuTe_2O_6$, this structure also has a similar 3D spin network of triangles formed by its first nearest neighbor (*nn*) and second *nn* couplings (see

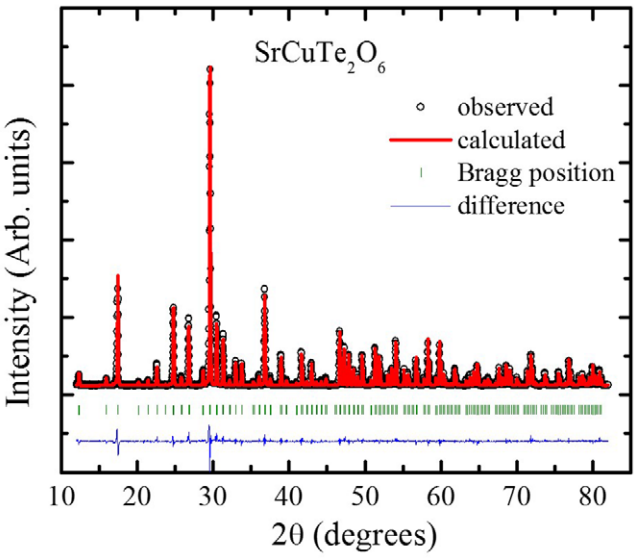

Figure 1. The Rietveld refinement of the powder x-ray diffraction pattern collected for $SrCuTe_2O_6$ at room temperature. The open circles (black) indicate the experimentally collected data, while the Rietveld refinement fit is shown as a red solid line. The Bragg positions and the difference curve are denoted by vertical green bars and a blue line, respectively. The residual parameters for the Rietveld refinement are $R_p \approx 4.388\%$, $R_{WP} \approx 6.469\%$, $R_{exp} \approx 2.369\%$, $R_{Bragg} \approx 3.235\%$, and goodness of fit (GOF) $= R_{WP}/R_p \approx 1.474$, respectively.

Table 1. The atomic coordinates and the occupancies obtained for $SrCuTe_2O_6$ after the Rietveld refinement at room temperature under the space group $P4_132$ (No 213).

Atom	Site	*x/a*	*y/a*	*z/a*	Occ.
Te	24e	0.338 73	0.918 45	0.061 53	1
Sr1	8c	0.057 61	0.057 61	0.057 61	1
Sr2	4b	0.375	0.625	0.125	1
Cu	12d	0.481 68	0.875	0.268 32	1
O1	24e	0.721 85	0.953 22	0.187 30	1
O2	24e	0.435 81	0.999 07	1.222 47	1
O3	24e	0.213 46	0.958 65	0.13565	1

figure 2(c)). The first *nn* distance between the Cu atoms is about 4.56 Å, while the second *nn* has a bond distance of about 5.52 Å. The magnetic couplings (J_1 and J_2) are mediated by the O–Sr2–O and O–Te–O paths, respectively. On the other hand, the third *nn* coupling forms the network of uniform chains via two possible paths (see figure 3(a) and table 2). One path is mediated through O–Sr2–O and the other is mediated through O–O. The coupling as a result of uniform chain interaction is denoted by J_3.

Despite the similar structure of $SrCuTe_2O_6$ and $PbCuTe_2O_6$, there are still some differences observed in the bond lengths and bond angles of the corresponding exchange couplings (see table 2). It is evident that the bond angles corresponding to J_2 (J_3) in the Sr-system are smaller (larger) than those of the Pb-system. This might suggest a relatively weaker J_2 (which was the strongest in the Pb-system) and a stronger J_3 in $SrCuTe_2O_6$. In addition, the Pb-system has two lone-paired elements (Pb^{2+} and Te^{4+}), whereas the Sr-system has only one lone-pair electron ion (Te^{4+}). These features might be responsible for the change in bond angles and bond lengths and thus might favor a different ground state for $SrCuTe_2O_6$.

3.2. Magnetic susceptibility $\chi(T)$

Magnetization, M, measurements were performed on the polycrystalline sample under a magnetic field (H) of 10 kOe in the temperature range 2–300 K, and the magnetic susceptibility $\chi(T)$ ($= M(T)/H$) versus T plot is depicted in figure 4(a). In sharp contrast to $PbCuTe_2O_6$ [17], the $\chi(T)$ data for $SrCuTe_2O_6$ exhibit a broad maximum at about 32 K, which signifies the presence of short-range correlations. In fact, it is quite surprising to observe such a broad maximum in a three-dimensional (3D) spin system (as anticipated from the structure). Generally the appearance of a broad maximum in the $\chi(T)$ data is a usual feature of the low-D (1D and 2D) spin systems.

Apart from the broad maximum at 32 K, the low temperature $\chi(T)$ data also evidence a sharp drop at 5.5 K ($=T_{N1}$), followed by a weak-kink at 4.9 K ($=T_{N2}$) measured with a field of 10 kOe. These transitions seem to be typical for an ordered antiferromagnetic system. The fitted $\chi(T)$ data to the Curie–Weiss law ($\chi_o + C/(T - \theta_{CW})$) in the T-range from 70 K to 300 K (not shown) yield temperature-independent susceptibility (χ_o), the Curie-constant ($C = Ng^2\mu_B^2 S(S+1)/3k_B$), and the Curie–Weiss temperature (θ_{CW}) to be $(1.30 \pm 0.05) \times 10^{-4}$ $cm^3\,mol^{-1}$-Cu, $(0.42 \pm 0.01)\,cm^3\,K\,mol^{-1}$-Cu, and $-(42 \pm 2)$ K, respectively. Here N_A, g, μ_B, and k_B are the Avogadro number, the Lande-g factor, the Bohr magneton, and the Boltzmann constant, respectively. For magnetic insulators, the temperature-independent magnetic susceptibility (χ_o) has two contributions. One is core diamagnetic susceptibility (χ_{dia}) and the other is Van-Vleck susceptibility (χ_{vv}). The diamagnetic susceptibility (χ_{dia}) of $SrCuTe_2O_6$ was calculated to be -1.52×10^{-4} $cm^3\,mol^{-1}$ Cu by summing up the individual diamagnetic susceptibilities of their ions Sr^{2+}, Cu^{2+}, and $(TeO_3)^{2-}$ [19]. The estimated Van-Vleck paramagnetic susceptibility $\chi_{vv}(= \chi_o - \chi_{dia})$ gives the value of 2.2×10^{-5} $cm^3\,mol^{-1}$, which is in good agreement with the other cuprates [20–22]. A negative θ_{CW} value suggests that spin interactions are of an antiferromagnetic nature. The estimated effective moment (μ_{eff}) value of Cu^{2+} is 1.83 μ_B, which is comparable to that of $S = 1/2$ (1.73 μ_B) moment.

In order to understand the ground state behavior of $SrCuTe_2O_6$ and the cause which drives the system into a different ground state other than that of $PbCuTe_2O_6$ is of paramount importance to understanding the behavior of the exchange couplings in this system. We looked at different models of isolated $S = 1/2$ triangular and $S = 1/2$ hyper-Kagome lattices (the first and second *nn* couplings as suggested by the structure) but none of the above models produce a broad maximum in their magnetic susceptibilities data. With the suspicion that the third *nn* coupling is the dominant one, we looked at the uniform chain model, which has a broad maximum in the magnetic susceptibility data. To support this reasoning, we also performed the LDA band structure calculations (explained in a later section) to find out the relative strengths of the exchange couplings. From the LDA

Table 2. A comparison between the bond angles and the bond lengths of the exchange couplings for $PbCuTe_2O_6$ and $SrCuTe_2O_6$.

		$SrCuTe_2O_6$		$PbCuTe_2O_6$	
Coupling	Paths for $SrCuTe_2O_6$	Bond length (Å)	Bond angle (°)	Bond length (Å)	Bond angle (°)
J_1	Cu–O–Sr2–O–Cu	4.56	O–Sr2–O ≈ 94.3	4.370	O–Pb2–O ≈ 91.3
J_2	Cu–O–Te–O–Cu	5.52	O–Te–O ≈ 92.5	5.60	O–Te–O ≈ 97
J_3	Cu–O–Sr2–O–Cu	6.29	O–Sr2–O ≈ 162.2	6.27	O–Pb2–O ≈ 156
	Cu–O–O–Cu	6.29 (O–O ≈ 2.78 Å)	Cu–O–O ≈ 154.4	(O–O ≈ 2.78 Å)	Cu–O–O ≈ 153.7

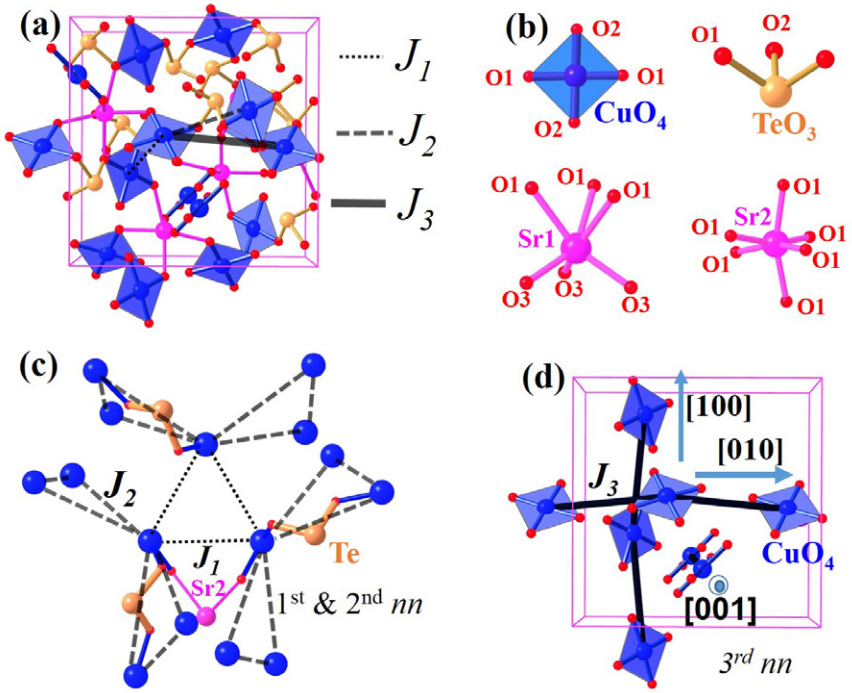

Figure 2. (a) Crystal structure of $SrCuTe_2O_6$ [16] (b) The environments of the CuO_4, TeO_3, $Sr1O_6$, and $Sr2O_6$ units. (c) Formation of the 3D network of corner-sharing triangles by the first *nn* and second *nn* coupled Cu-atoms. (d) Formation of uniform chains by the third *nn* coupling, passing along all the crystallographic (*a*, *b*, and *c*) directions.

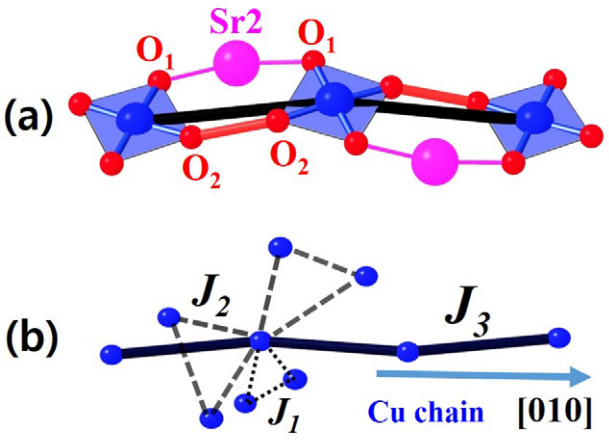

Figure 3. (a) The details of the uniform spin chain formed by the third *nn* coupling (J_3). (b) The uniform spin chain with its associated frustrated inter-chain couplings (J_1 and J_2).

calculations, we found that the major interaction coupling is the third *nn*, which essentially forms a network of uniform chains, propagating along all three crystallographic (*x*-, *y*-, and *z*-) axes, as shown in figure 2(d). Having identified the third *nn* coupling as the leading exchange interaction in our system, we finally analyzed our magnetic data in the framework of the $S = 1/2$ uniform spin chain model [23]. A successive appearance of anomalies below 5.5 K is an indication of the involvement of the inter-chain couplings. So, in view of this fact the data were finally fitted to the coupled $S = 1/2$ uniform chain with the mean-field approach (equation (1)) down to 12 K, taking the inter-chain couplings into consideration.

$$\chi = \chi_o + \frac{(J_3, T)}{1 + \frac{ZJ'}{Ng^2\mu_B^2}(J_3, T)}, \tag{1}$$

The values of uniform intra-chain coupling J_3/k_B and the total strength of inter-chain coupling ZJ' are found to be (43 ± 2) K and (13 ± 1) K, respectively. The obtained value J_3/k_B is slightly smaller than the expected value for a 1D chain with a broad maximum 32 K (= 0.640 851 $J_3/k_B \approx 50$ K) [23]. This disparity could be due to the influence of inter-chain interactions. The presence of inter-chain interactions leads to a shift in the position of the broad-maximum in the susceptibility [38]. On the other hand, the finite size effects also influence

the position of the broad maximum. To calculate the inter-chain coupling (ZJ') just by exploiting the values of T_N and J_{chain} using the following expression (2) [23]

$$ZJ' = \frac{T_N}{0.2333\sqrt{\ln\left(\frac{2.6J_3}{T_N}\right) + \frac{1}{2}\ln\left(\ln\left(\frac{2.6J_3}{T_N}\right)\right)}}. \quad (2)$$

The estimated value of $ZJ' \sim 12$ K comes very close to the previously obtained value from the expression (1).

3.3. Heat capacity (C_p) in zero field

The T-dependent heat capacity C_p of the polycrystalline $SrCuTe_2O_6$ sample in zero-field is shown in figure 4(b). Being a magnetic insulator, $SrCuTe_2O_6$ has two contributions to C_p, namely, lattice and magnetic. Due to the lack of availability of the non-magnetic analog of $SrCuTe_2O_6$, we used the Debye model [24] to extract the lattice contribution of the C_p data. We found that a linear combination of two Debye integrals results in the best fit to the C_p data. The data are fitted successfully in the T-range from 40 to 130 K using the following equation mentioned in the text.

$$C_p = 9rNk_B \sum_{i=1,2} C_i \left(\frac{T}{\theta_D^i}\right)^3 \int_0^{x_D^i} \frac{x^4 e^x}{(e^x - 1)^2} dx. \quad (3)$$

Here r is the number of atoms per formula unit and θ_D is a Debye temperature. The fitting yields $C_1 \approx (0.3 \pm 0.05)$, $\theta_{D1} \approx (171 \pm 5)$ K, $C_2 \approx (0.46 \pm 0.05)$, and $\theta_{D2} \approx (562 \pm 10)$ K. The fitted curve was then extrapolated down to 2 K and subtracted it from the measured $C_p(T)$ data. As a consequence, the obtained magnetic heat capacity $C_m(T)$ is shown in the inset (ii) of figure 4(b). Similar to the $\chi(T)$ data, two sharp and distinctive anomalies are observed, as can also be seen on the plot of C_p/T^2 versus T (inset (i) of figure 4(b)). The data follow T^3 behavior at low-T, as expected for AFM ordered spin systems, which are contrary to the T^2 behavior observed in $PbCuTe_2O_6$.

We observed a broad maximum (T^{max}) at 15 K in the $C_m(T)/T$ data, which is expectedly lower than the value of the broad maximum at 32 K in the χ data. This feature has already been seen in several low-D spin systems [23, 25]. The observed values of T^{max} and $(C_m/T)^{max}$ also provide a way of estimating the exchange energy couplings in the system using the theoretical equations given below for the 1D model. These values are nearly in agreement with the value estimated from the χ data.

$$(T_{max})^{C_m/T} = 0.307\left(\frac{J_3}{k_B}\right) \quad (4)$$

$$(C_m/T)^{max} = 0.8973651\frac{Nk_B^2}{J_3}. \quad (5)$$

The obtained values are found to be $J_3/k_B \approx 43$ K and 38 K, respectively. The small disagreement observed in the above estimated values might be due to the error in estimating the magnetic heat capacity.

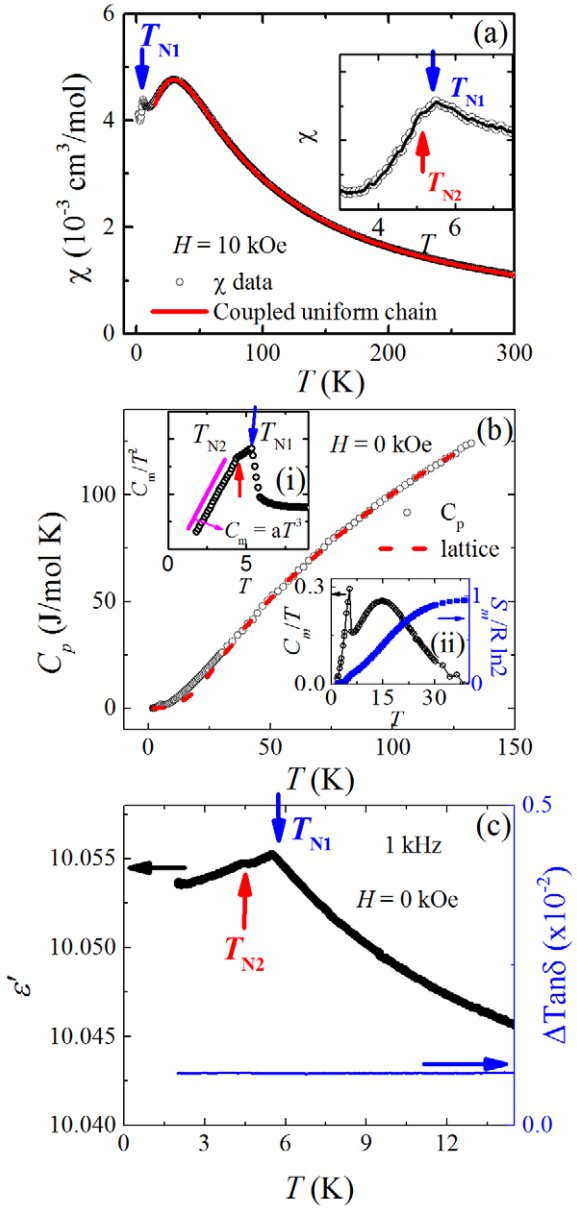

Figure 4. (a) Magnetic susceptibility χ versus temperature T with a fit to a coupled $S = 1/2$ uniform chain model (red solid line). The inset shows the appearance of two transitions T_{N1} and T_{N2} at low temperatures. (b) Zero field C_p with a fit to the lattice contribution. The inset (i) shows the plot of C_m/T^2 versus T. The inset (ii) shows the plot of C_m/T (left-axis) and the normalized magnetic entropy change S_m/Rln2 (right-axis) versus T. (c) The plot of the real part of the dielectric constant (left-axis) and dissipation factor (right-axis) versus T. The dissipation factor or loss tangent (the ratio of the imaginary and real part of the dielectric constant) can be used to extract the imaginary part. The two transition temperatures T_{N1} and T_{N2} are indicated by down and up arrow marks, respectively.

The entropy change S_m calculated from the magnetic heat capacity is found to be 5.5 J mol^{-1} K^{-1}, which is very close to the expected value Rln2 for $S = 1/2$ systems (see the inset (ii) of figure 4(b)). The S_m value at transition T_{N1} is found to be ≈ 0.6 J mol^{-1} K^{-1}, which is only about 10% of the total entropy, and the rest of the entropy is recovered in the paramagnetic region up to the θ_{CW} temperatures (well above T_N).

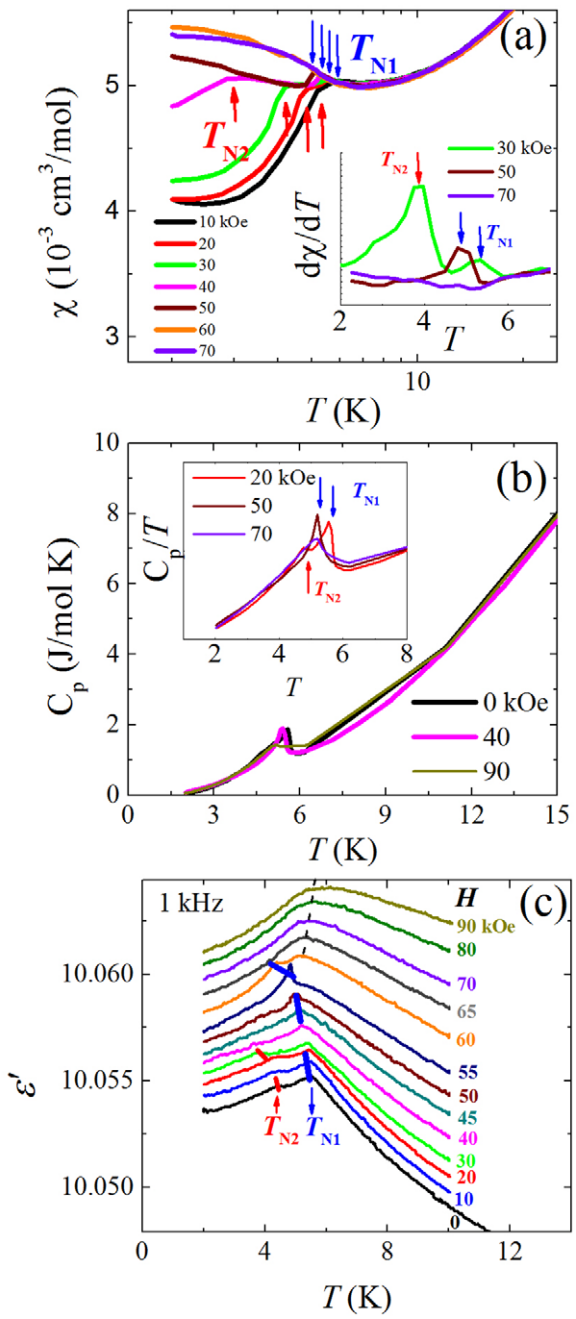

Figure 5. (a) $\chi(T)$ data in different magnetic fields from 10 to 70 kOe. The inset of (a) shows the plot dχ/dT versus T. (b) The main (inset) plot shows $C_p(C_p/T)$ versus T for different fields up to 90 kOe. (c) The plot of the dielectric constant (ε') versus T in different Hs up to 90 kOe. The two transitions T_{N1} and T_{N2} are indicated by down and up arrows, respectively.

This is also an indication of the presence of short-range correlations in the paramagnetic region.

3.4. Dielectric constant $\varepsilon'(T)$ in zero field

Figure 4(c) displays the temperature dependence of dielectric constant, $\varepsilon'(T)$, of $SrCuTe_2O_6$ measured in zero field. As T decreases, the $\varepsilon'(T)$ increases and shows a cusp-like anomaly at 5.5 K, followed by another anomaly at 4.5 K, respectively. This is in good agreement with the magnetic anomalies previously seen in the $\chi(T)$ and $C_p(T)$ data in zero field. The dielectric loss (ΔTanδ) is found to be less than 0.1%, which is almost negligible. The simultaneous appearance of these transitions in the $\varepsilon'(T)$, $C_p(T)$, and $M(T)$ data suggests the presence of magneto-dielectric behavior, which is usually a common feature for magneto-dielectric materials. For example, $CuTeO_3$, $CuSeO_3$, etc [26] also show a similar cusp-like behavior, but it is rather different from the λ-like peak feature noticed for other multiferroics, where the spontaneous ferroelectricity P appears below the transition temperature. The absence of pyrocurrent below this transition probably hints at the absence of spontaneous ferroelectricity in this system in zero field.

3.5. $M(T)$, $C_p(T)$, and $\varepsilon'(T)$ in magnetic fields

To know more about the nature of low-T AFM and dielectric transitions, we measured $M(T)$, $C_p(T)$, and $\varepsilon'(T)$ in different magnetic fields ranging from 10–90 kOe. The $\chi(T)$ data in different magnetic fields are shown in figure 5(a). The $\chi(T)$ data show a field-dependent behavior below about 60 kOe and T_{N1} and T_{N2} gradually move to the lower temperatures on increasing the magnetic field. However, T_{N2} shifts rapidly towards the low-T side with the applied fields and is finally suppressed by a magnetic field of about 40 kOe (called H_{C1}). Similarly, the other anomaly T_{N1} is also suppressed by 60 kOe (called H_{C2}). To exaggerate the anomalies at low temperatures, the derivative plot of χ with respect to T (i.e. dχ/dT) is shown in the inset of figure 5(a). In this plot, the 30 kOe data have two peaks corresponding to T_{N1} and T_{N2}; however, at 50 kOe the peak corresponding to T_{N1} remains and T_{N2} is suppressed completely. Finally, at 70 kOe the peak associated with T_{N1} also disappears and the data leftover with a small dip at 5.3 K.

Similar behavior is also observed in the $C_p(T)$ and $\varepsilon'(T)$ data measured with different fields, as shown in figures 5(b) and (c), respectively. Similar to the magnetic data, the C_p/T data at 20 kOe also show two distinctive peaks corresponding to T_{N1} and T_{N2} (see the inset of figure 5(b)). Having suppressed T_{N2} by a field of 40 kOe, the data of C_p/T at 50 kOe are left only with a single sharp peak. When the field was increased up to 70 kOe, the magnitude of the peak at T_{N1} suddenly dropped and the peak became broader. This very feature indicates a change in the antiferromagnetic nature of T_{N1} in this region, and on further increasing the field above 70 kOe, not much change in the shift or the shape of the peak was observed. Here we note that this robust peak survives in C_p for $H > 70$ kOe, whereas such a peak was not found in the magnetic data. We suspect that the peak might be hidden under the Curie behavior in the magnetic data (see figure 5(a)). In order to reassure the $\chi(T)$ and $C_p(T)$ findings, we also performed $\varepsilon'(T)$ in a field range 0–90 kOe. The results of $\varepsilon'(T)$ nearly match with the C_p and χ data. Likewise, the shift in the peak position and the difference in the shape of the anomalies with the applied magnetic fields at different regions are shown in figure 5(c).

3.6. $M(H)$, $\varepsilon'(H)$ at different temperatures

To unveil this field-induced magnetic behavior, we measured $M(H)$ isotherms at different temperatures from 2 to 5 K (see

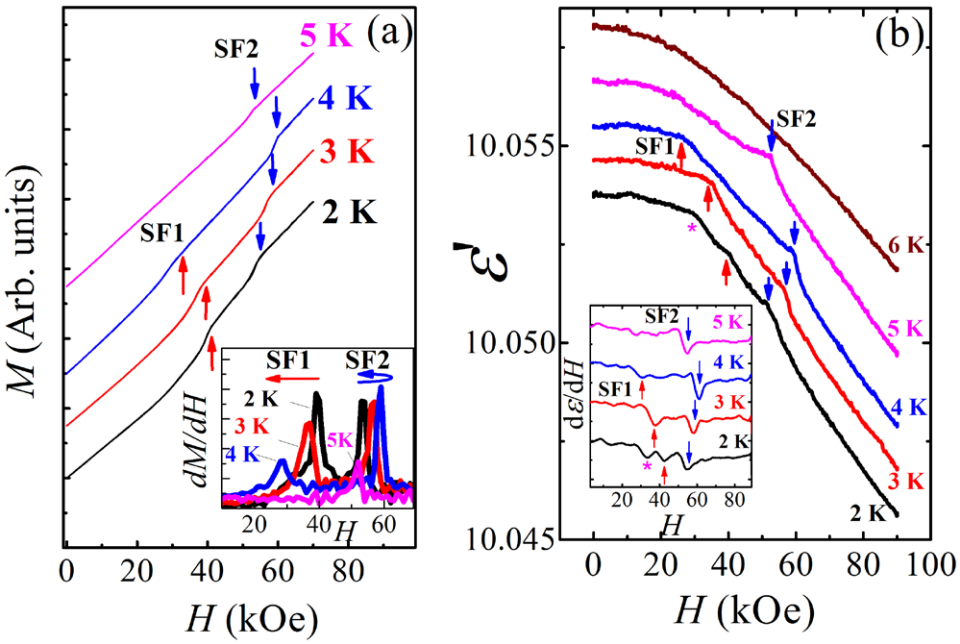

Figure 6. (a) The magnetization (M) versus the H plot at different temperatures and the inset of (a) shows the derivative plot of magnetization (dM/dH) versus H. (b) Shows the dielectric constant (ε') versus the H plot for various Ts from 2 to 6 K and the inset represents the $d\varepsilon'/dH$ versus the H plot. The vertical up and down arrow marks indicate the change in their slopes marked by SF1 and SF2, respectively. The (*) symbol indicates a change in the slope of the ε' data, but the corresponding change is not seen in the magnetic data.

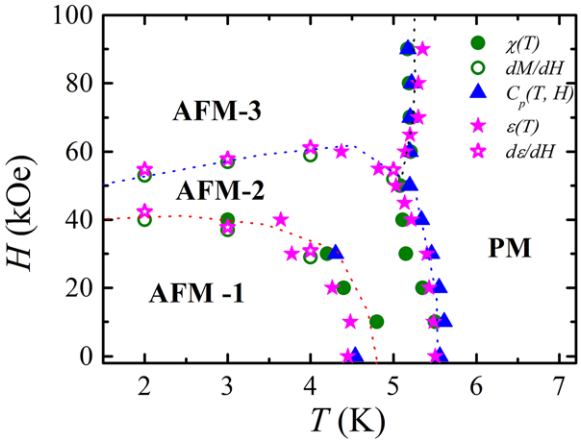

Figure 7. Evolution of different antiferromagnetic (AFM) regions (AFM-1, AFM-2 & AFM-3) and their separation from the paramagnetic (PM) phase is depicted as a function of magnetic field and temperature.

figure 6(a)). At 2 K, $M(H)$ shows two jumps at the fields of about 40 kOe (SF1) and 53 kOe (SF2), respectively, and suggests that these field-induced transitions are due to the reorientations of the spins in the ordered state; as a result they seem to be spin-flop transitions. The SF1 decreases as T increases and finally disappears at T above 4 K, while the SF2 increases first and then again decreases with T. This behavior can be clearly seen in dM/dH versus the H plot in the inset of figure 6(a). The field-induced spin-flop transitions SF1 and SF2 are absent in the $M(H)$ data at temperatures above T_{N1}. The value of the fields at which the observed SF1 and SF2 are nearly equal to the value of the critical fields H_{C1} and H_{C2}, (fields at which the T_{N2} and T_{N1} are suppressed in the $\chi(T)$), respectively. This again suggests that the observed field-induced transitions (T_{N1} and T_{N2}) are rather related to these spin-flop transitions. Similar behavior is also observed in the $\varepsilon'(H)$ and $d\varepsilon'/dH$ data at different temperatures, as shown in figure 6(b) and its inset.

3.7. Magnetic phase diagram

From magnetization (M), heat capacity (C_p), the dielectric constant (ε') data, and their derivatives with respect to H and T's, a magnetic phase-diagram is built, as shown in figure 7. The magnetic phase-diagram separates the boundary between the paramagnetic (PM) and antiferromagnetic (AFM) regions. Also, it has been identified that the AFM region comprises different phases AFM-1, AFM-2, and AFM-3, which are found to be tuned by the external magnetic field. A detailed neutron diffraction study would be needed to understand the spin orientations of these local AFM regions.

3.8. Electronic structure calculations

In order to understand the magnetic behavior and the basic electronic structure, we have carried out density functional theory calculations using the Vienna Ab-initio Simulation Package (VASP) code [27, 28] within the projector augmented-wave (PAW) method [29, 30]. The exchange and correlation effects are treated using the local density approximation (LDA). The kinetic energy cut off the plane wave basis was chosen to be 600 eV. Brillouin-zone integration was performed using a $4 \times 4 \times 4$ k-mesh.

Figure 8(a) shows the non-spin polarized band dispersion of $SrCuTe_2O_6$ along various high symmetry directions of the Brillouin zone corresponding to the cubic lattice. The most important feature of the band structure is the isolated manifold

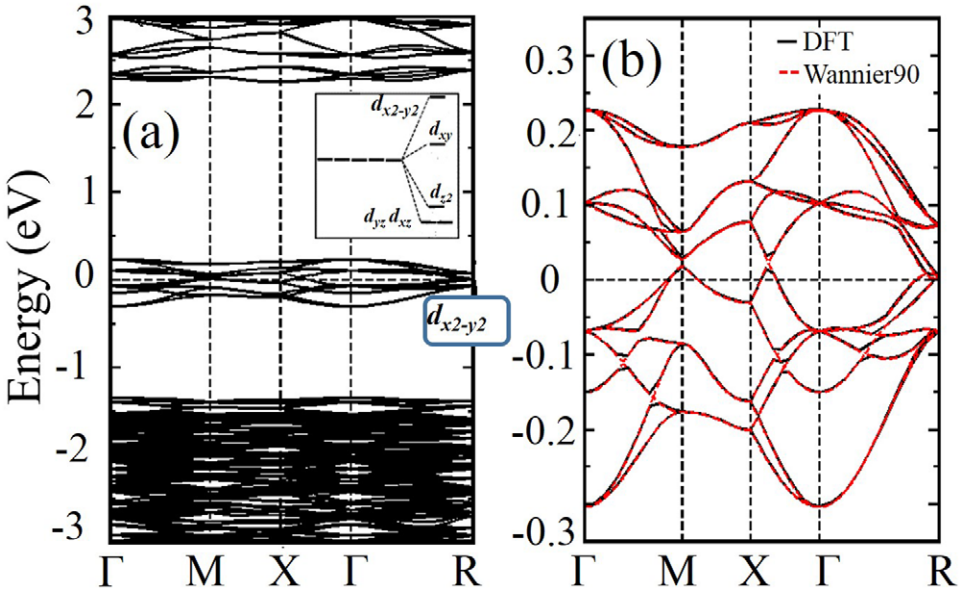

Figure 8. (a) Non-spin polarized band dispersion along various high symmetry directions. The inset shows the crystal field splitting corresponding to a square planar environment. (b) Superimposed Wannier-interpolated bands on the LDA bands.

Table 3. The hopping integrals and the exchange interaction between the Cu ions.

Hopping	Cu–Cu distance (Å)	Hopping parameters (meV)	$J_i/J_3 = (t_i/t_3)^2$	Exchange interactions
t_1	4.55	13.99	0.03	1.36
t_2	5.52	26.54	0.11	5.03
t_3	6.29	79.92	1.00	45.60

of twelve bands near the Fermi level (E_F), which arises from the twelve Cu atoms in the unit cell. These bands are predominantly of Cu d_{x2-y2} character in the local frame of reference, where the Cu atom is at the square planar environment of O atoms. The crystal field splitting corresponding to a square planar environment is shown in the inset of figure 8(a). Since Cu is in d^9 configuration, these isolated bands are half filled and separated from the other Cu d bands by a gap of 1.1 eV (see figure 8(a)), and hence these bands are responsible for the low-energy physics of the material.

To extract a low-energy model Hamiltonian, we construct the Wannier function for the d_{x2-y2}-like bands, using the VASP2WANNIER and WANNIER90 codes [31].

Figure 8(b) displays the superimposed Wannier-interpolated bands on the LDA bands and the agreement is quite remarkable. The various hopping interactions (t_n) obtained with this method are shown in table 3. Since the only relevant orbital is d_{x2-y2}, which is half filled, Cu at different sites can only interact via the super-exchange mechanism. The super-exchange interactions between the Cu ions at different sites have been estimated using the relation $J = 4t^2/U_{\text{eff}}$, where U_{eff} is the effective onsite Coulomb interaction. Since a constrained DFT calculation by Anisimov *et al* [32] for $CaCuO_2$ gives $U_{\text{eff}} = 6.5$ eV for the Cu ions, where Cu is in the same charge state 2 + as in the present system, we choose this value for the estimation of J. Our estimated J (see table 3) clearly reveals that the third *nn* exchange interaction (J_3) is the most dominant one. To understand why J_3 is the most significant interaction in this system, we analyze

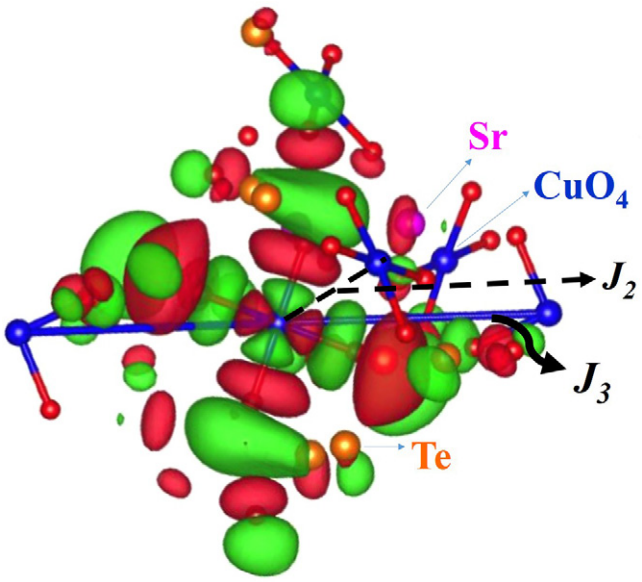

Figure 9. Wannier function plot of effective Cu d_{x2-y2} orbitals.

the interesting crystal geometry of this system. The third *nn* Cu atoms interact via the Cu–O–O–Cu path with the O–O bond (see figure 3(a)) and hence the third *nn* Cu forms a 1D chain. The Cu d_{x2-y2} strongly hybridizes with the O p_x orbital via bonding O–O, which mediates the Cu ions close to each other. As a consequence, Cu d_{x2-y2}–Cu d_{x2-y2} hopping

has become the most significant for the third *nn*, as is also shown in the Wannier plot (see figure 9). We also found that the next dominant interaction is the second *nn* (J_2), which is relatively small ($\approx 0.1J_3$) and also frustrated; hence, this can only play a significant role at low temperatures. As shown in table 3, the remaining interactions are very small and do not play any decisive role in the magnetism of this system. Since J_2 is quite small and (1/10)th of J_3, we can consider the $SrCuTe_2O_6$ as a 1D uniform chain with very small frustrated inter-chain interactions.

From the values obtained from the LDA calculations, one can estimate the total strength of the inter-chain interactions $ZJ' = (z_1J_2 + z_2J_2) \approx 0.5J_3$. According to the uniform chain model with unfrustrated inter-chain couplings (equation (2)), this value is supposed to have a T_{N1} value of about 17 K, which is, in fact, very much larger than that of the experimentally observed value of 5.5 K ($\approx T_{N1}$). This disagreement suggests that the inter-chain interactions in $SrCuTe_2O_6$ are in the frustrated nature, which results in a smaller T_{N1} value. These kinds of differences are also observed for several other spin chains with frustrated inter-chain couplings; e.g. Ca_2CuO_3 [33, 34], $Sr_2Cu(PO_4)_2$ [35, 36], $K_2CuP_2O_7$ [37] etc. We also note that the mismatch could be partly due to the limitations of our mean-field approach analysis.

However, we did not observe any electric polarization $\leqslant T_{N1}$ in this material unlike the other intra-chain frustrated, multiferroic chain materials [5–12]. This might be due to the lack of sufficient strong inter-chain couplings (J_2/J_3 is about 0.1) in this material. A further theoretical study is required to find out the origin of the magneto-dielectric behavior in this material.

4. Conclusion

We have studied the magnetic properties of a new chain material $SrCuTe_2O_6$ via magnetic specific heat, as well as dielectric constant measurements and electronic structure calculations. However, the crystal structure of $SrCuTe_2O_6$ is similar to its sister compound $PbCuTe_2O_6$, but due to the dominant third *nn* exchange coupling the ground state exhibits the characteristic features of 1D magnetism. The magnetic data analysis well corroborated by the LDA band structure calculations also suggests the presence of uniform chains with non-negligible frustrated inter-chain couplings (J_1 and J_2), which might lead to magneto-dielectric anomalies observed at low-T (5.5 and 4.5 K). Magnetic field induced phases are also observed in the antiferromagnetically ordered region. The magnetic phase diagram built on behalf of the magnetization, heat capacity, and dielectric constant experiments evidences the presence of different AFM regions. We note that recently a similar magnetic phase diagram was reported using magnetization and heat-capacity measurements [39]. The determination of the magnetic structures of these phases by neutron diffraction would be within the scope of a future study to explore the associated mechanism of the magneto-dielectric effect in this new type of $S = 1/2$ chain material with frustrated inter-chain interactions.

Acknowledgments

BK thanks the DST INSPIRE faculty award-2014 scheme. FCC acknowledges the support from the Ministry of Science and Technology in Taiwan under project number MOST-102-2119-M-002-004. AVM thanks the Department of Science and Technology, the Government of India for their financial support. R Kumar acknowledges the IRCC IITB grant for financial support. The work at SNU was supported by the National Creative Research Initiative (2010-0018300). We thank Patrick Lee for fruitful discussions.

References

[1] Mermin D and Wagner H 1966 *Phys. Rev. Lett.* **17** 1133
[2] Majumdar C K and Ghosh D K 1969 *J. Math. Phys.* **10** 1399
[3] Bursill R, Gehring G A, Farnell D J J, Parkinson J B, Xiang T and Zeng C 1995 *J. Phys.: Condens. Matter* **7** 8605
[4] Dmitriev D V and Krivnov V Y 2006 *Phys. Rev.* B **73** 024402
[5] Park S, Choi Y J, Zhang C L and Cheong S-W 2007 *Phys. Rev. Lett.* **98** 057601
[6] Gibson B J, Kremer R K, Prokofiev A V, Assmus W and McIntyre G J 2004 *Physica* B **350** e253
Enderle M *et al* 2005 *Europhys. Lett.* **70** 237
[7] Drechsler S-L *et al* 2007 *Phys. Rev. Lett.* **98** 077202
[8] Banks M G, Kremer R K, Hoch C, Simon A, Ouladdiaf B, Broto J-M, Rakoto H, Lee C and Whangbo M-H 2009 *Phys. Rev.* **80** 024404
[9] Seki S, Kurumaji T, Ishiwata S, Matsui H, Murakawa H, Tokunaga Y, Kaneko Y, Hasegawa T and Tokura Y 2010 *Phys. Rev.* B **82** 064424
[10] Zhao L *et al* 2012 *Adv. Mater.* **24** 2469
[11] Lee C, Liu Jia, Whangbo M -H, Koo H -J, Kremer R K and Simon A 2012 *Phys. Rev.* B **86** 060407
[12] Law J M, Reuvekamp P, Glaum R, Lee C, Kang J, Whangbo M-H and Kremer R K 2011 *Phys. Rev.* B **84** 014426
[13] Tarui Y, Kobayashi Y and Sato M 2008 *J. Phys. Soc. Japan* **77** 043703
[14] Katsura H, Onoda S, Han J H and Nagaosa N 2008 *Phys. Rev. Lett.* **101** 187207
[15] Furukawa S, Sato M, Saiga Y and Onoda S 2008 *J. Phys. Soc. Japan* **77** 123712
[16] Wulf L and Mueller-Buschbaum H 1997 *Z. Naturforsch.* B **52** 1341
[17] Koteswararao B *et al* 2014 *Phys. Rev.* B **90** 035141
[18] Rodríguez-Carvajal J 1993 *Physica* B **192** 55
[19] Selwood P W 1956 *Magnetochemistry* 2nd edn (New York: Wiley-Interscience) p 78 chapter 2
[20] Motoyama N, Eisaki H and Uchida S 1996 *Phys. Rev. Lett.* **76** 3212
[21] Koteswararao B *et al* 2012 *J. Phys.: Condens. Matter* **24** 236001
[22] Koteswararao B, Kumar R, Chakraborty J, Jeon B-G, Mahajan A V, Dasgupta I, Kim K H and Chou F C 2013 *J. Phys.: Condens. Matter* **25** 336003
[23] Johnston D C, Kremer R K, Troyer M, Wang X, Klümper A, Bud'ko S L, Panchula A F and Canfield P C 2000 *Phys. Rev.* B **61** 9558
[24] Kittel C 1996 *Introduction to Solid State Physics* (Singapore: Wiley)
[25] Koteswararao B, Salunke S, Mahajan A V, Dasgupta I and Bobroff J 2007 *Phys. Rev.* B **76** 052402
[26] Lawes G, Ramirez A P, Varma C M and Subramanian M A 2003 *Phys. Rev. Lett.* **91** 257208

[27] Kresse G and Hafner J 1993 *Phys. Rev.* B **47** 558
[28] Kresse G and Furthmuller J 1996 *Phys. Rev.* B **54** 11169
[29] Blöchl P E 1994 *Phys. Rev.* B **50** 17953
[30] Kresse G and Joubert D 1999 *Phys. Rev.* B **59** 1758
[31] Mostofi A A, Yates J R, Lee Y-S, Souza I, Vanderbilt D and Marzari N 2008 Wannier90: a tool for obtaining maximally-localised wannier functions *Comput. Phys. Commun.* **178** 685
[32] Anisimov V I, Zaanen J and Andersen O K 1991 *Phys. Rev.* B **44** 943
[33] Rosner H, Eschrig H, Hayn R, Drechsler S-L and Málek J 1997 *Phys. Rev.* B **56** 3402
[34] Kojima K M *et al* 1997 *Phys. Rev. Lett.* **78** 1787
[35] Johannes M D, Richter J, Drechsler S-L and Rosner H 2006 *Phys. Rev.* B **74** 174435
[36] Nath R, Mahajan A V, Büttgen N, Kegler C and Loidl A 2005 *Phys. Rev.* B **71** 174436
[37] Nath R, Kasinathan D, Rosner H, Baenitz M and Geibel C 2008 *Phys. Rev.* B **77** 134451
[38] Johnston D C *et al* 2000 arXiv:cond-mat/0001147
[39] Ahmed N, Tsirlin A A, and Nath R 2015 *Phys. Rev.* B **91** 214413